ACS APPLIED MATERIALS & INTERFACES

Research Article

www.acsami.org

Solvothermal Synthesis of ZnO Nanostructures and Their Morphology-Dependent Gas-Sensing Properties

Prabhakar Rai, Woon-Ki Kwak, and Yeon-Tae Yu*

Division of Advanced Materials Engineering and Research Centre for Advanced Materials Development, College of Engineering, Chonbuk National University, Jeonju 561-756, South Korea

Supporting Information

ABSTRACT: Single-crystalline ZnO nanostructures were synthesized by solvothermal method using methanol as solvent. The effect of counterions of zinc salts (nitrate, acetate, and chloride) on the morphology of ZnO nanostructures was investigated. ZnO nanorods (NRs) were formed for all kinds of zinc salts except zinc chloride, where nanoparticles (NPs) were formed. The length and width of ZnO NRs were 100–150 nm and 20–25 nm, respectively, whereas NPs were 20–25 nm in diameter. Replacing methanol to ethanol generated only NRs for all kinds of zinc salts and they were about 10 times larger than those in methanol. The effect of morphology on sensing property was investigated by comparing their response. ZnO NRs showed very high response as compared to ZnO NPs for NO_2 and vice versa for CO, although the surface area of ZnO NPs (42.83 m^2/g) was much higher than those of ZnO NRs (17.6 m^2/g). The response of ZnO NRs was 30 times higher than those of NPs for NO_2 gas, whereas 4 times lower for CO gas. The maximum response of as prepared ZnO NRs was 44.2 to 50 ppm of NO_2 gas at 300 °C. A relationship between morphology and interelectrode gap was established. It was demonstrated that the number of grains present between interelectrode gaps has significantly affected the response.

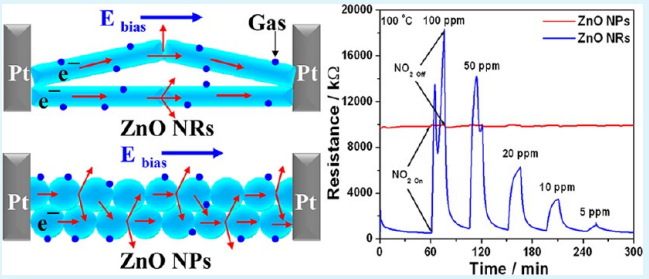

KEYWORDS: *ZnO, nanostructures, single crystalline, interelectrode gap, gas sensor, NO_2*

INTRODUCTION

Metal oxides as sensing material in chemical sensors have been used for a long time as a low cost alternative for gas detection devices. However, compared to more expensive alternatives, they suffered from limitations in sensitivity, selectivity, and stability. Gas sensing is a kind of surface phenomenon, which involves gas–solid interaction that occurs at the sensor surface. Therefore, their performance is governed by the exposed surface area, which means increasing the active surface area will likely increase the sensor performance. Recent development in fabrication techniques of nanomaterials has improved the performance of these materials.[1,2] Many recent reports have shown that by carefully controlling the nanostructure of metal oxide sensing layers greatly improved sensing properties.[3,4] Mostly, metal oxide sensing layer is produced by thermal treatment of the film over 300 °C, which, unfortunately, causes grain growth and has a detrimental effect on the surface to volume ratio of the sensing layer.[5] However, nanostructures that exhibit a high degree of crystallinity suffer less from this drawback and should enable production of sensor devices with good long-term stability.[2,6,7] Growth of one-dimensional nanostructure, such as NRs, nanowires, and nanobelts has enhanced sensor qualities because of the high surface to volume ratio.[2,8] As an important II–VI semiconductor, ZnO has attracted great interests in electronics and optoelectronics owing to its unique properties, such as wide band gap (3.37 eV) and large exciton binding energy (60 meV).[9–11] ZnO is known for its stability under harsh processing conditions and is also listed as generally regarded as safe (GRAS) for human beings.[12] Therefore, extensive work is going on for its environmental applications like photocatalysis, gas sensor and antibacterial activity.[13–15] These properties are surface related phenomenon, and hence nanosized ZnO is receiving ever-increasing attention because of its high surface area. Recently, 1D ZnO nanostructures like NRs, nanowires, nanofibers, etc., have been receiving much attention because of their high surface to volume ratio.[16–18]

Furthermore, the process of gas sensing by a semiconductor device involves two key functions, i.e., receptor and transducer function.[19] Receptor function involves the recognition of a target gas through a gas–solid interaction, which induces an electronic change of the oxide surface, whereas transducer function involves the transduction of the surface phenomenon into an electrical resistance change of the sensor. Receptor function depends on surface area, structural defects, impurities, etc., and in general, their presence improves the recognition of the gas molecules. On the other hand, transducer function strongly depends on the morphology of the sensitive layer as well as the contribution of interfaces between metal oxide particles and underlying metal electrodes and those between

Received: November 23, 2012
Accepted: March 22, 2013
Published: March 22, 2013

oxide particles in polycrystalline materials. Therefore, gas-sensing property depends not only on sensing material characteristics but also contact resistance between sensing material and electrodes. Meanwhile, recent advances in the field of metal oxide gas sensor have been mostly related to receptor function, such as shape and size control, introduction of a catalyst like noble metals, etc. However, the effect of materials engineering on transducer factor is rarely investigated.[20−25] In view of this, we report a study of the sensing capabilities of different types of ZnO sensing layers (NRs and NPs). The main focus of this study is to investigate the influence of morphology on the gas sensing capabilities, taking an inter electrode gap into account. ZnO NPs and NRs both have the same phase, structural defects, and diameter, and differ in their morphology and surface area. It is found that the response of ZnO NPs is poorer than NRs for NO_2 and vice versa for CO gas, although ZnO NPs have a larger surface area than NRs. It is demonstrated that the numbers of grains present between interelectrode gaps have significant effect on the resistance of sensors and consequently their response.

MATERIALS AND EXPERIMENTAL PROCEDURE

Synthesis of ZnO Nanostructures. ZnO nanostructures were synthesized by solvothermal method.[18] In a typical procedure, 0.1 M $Zn(NO_3)_2{\cdot}6H_2O$ (Reagent grade, 98% Sigma-Aldrich) and 0.5 M NaOH solution was prepared by dissolving in 10 and 20 mL of methanol, respectively. These two solutions were mixed, followed by vigorous stirring for 1 h in ice bath. After being stirred, the resultant solution was transferred in to a Teflon-lined stainless-steel autoclave with volume of 50 mL, and subsequently sealed and heated at 120 °C for 24 h. After completion of the reaction, it was allowed to cool down at room temperature. The product was centrifuged and washed with deionized water and ethanol, then freeze-dried for 12 h, for further investigations. A similar procedure was also carried out for the synthesis of ZnO nanostructures in ethanol with their different zinc salts such as zinc acetate (99%, SHOWA Chemicals Co. Ltd.) and zinc chloride (98%, JUNSEI).

Characterization. The crystallographic structures of the solid samples were determined using a D/Max 2005 Rigaku X-ray diffractometer equipped with graphite monochromatized high-intensity Cu−K < alpha >1 radiation (λ = 1.5405 Å). The X-ray diffraction (XRD) patterns were recorded from 30 to 70° (2θ) with a scanning speed of 0.04° s^{-1}. The particle size and morphology was investigated by field emission scanning electron microscopy (FESEM; Carl Zeiss SUPRA) and transmission electron microscopy (TEM; JEM-2010, JEOL). The corresponding fast Fourier transfer (FFT) patterns were obtained using the Digital Micrograph (DM) software to treat the related high resolution TEM (HRTEM) images. Optical property was investigated by UV−visible spectroscopy (UV-2550; Shimadzu) and photoluminescence (PL) spectroscopy at 325 nm excitation wavelength using Cd−He laser. The surface area was analyzed by Brunauer−Emmett−Teller (BET) surface area analyzer (TriStar, Micromeritics).

Gas-Sensing Measurements. To measure the sensor response of these ZnO nanostructures, a sensor device was prepared as reported in our previous work[26] (also see Figure S1 in the Supporting Information). ZnO powder (0.1g) was mixed with α-terpineol (500 μL) and grinded in an agate mortar for 30 min. The ZnO paste was pasted by doctor blading method onto the cleaned alumina circuit board with interdigitated platinum electrodes. The size of alumina circuit board was 15 mm × 15 mm. In this circuit board platinum electrode were interdigitated in the area of 10 mm × 10 mm. The spacing between two electrodes was 237 μm, measured by SEM. The device was dried at 80 °C for 5 h. The ZnO-loaded device was sintered at 500 °C in a muffle furnace for 5 h. The change in resistance of the device, due to the presence of test gas, was measured using a high resistance meter (Agilent 34970A). Resistance meter was connected to the computer via a KUSB-488A interface to record the signal due to change in resistance. The device was tested in the temperature range of 50 to 400 °C for various concentrations of NO_2 (5−100 ppm) and CO (200−1000 ppm) in a temperature-controlled environment. The balance gas was N_2, and the dry air was mixed to be 10.5% of oxygen. The total gas flow rate was 100 cm^3/min. The sensor response (R_s) was calculated using (R_g/R_a) for NO_2 and (R_a/R_g) for CO gas. Here, R_a is the resistance in dry air with 10.5% O_2, and R_g is the resistance in the test gas.

RESULTS AND DISCUSSION

Structural Properties. FESEM images of ZnO nanostructures synthesized in different solvents using various zinc salts are shown in Figure 1. It shows that ZnO NRs synthesized in ethanol medium are much larger than those in methanol medium. The ZnO synthesized in ethanol medium from zinc nitrate are nonuniform and larger (1−5 μm) as compared to acetate (1−1.5 μm) and chloride (1−1.5 μm) counterparts. However, in methanol medium the shape and size of ZnO NRs are almost same for those synthesized from zinc nitrate and acetate, except for chloride. The length and width of these ZnO NRs are 100−150 and 20−25 nm, respectively. For zinc chloride, NPs with 20−25 nm diameters are formed in methanol medium. The growth habit of ZnO under hydrothermal condition has been investigated.[27] ZnO is a polar crystal and overall shape and aspect ratio of crystals are determined by the relative rates of growth of its various faces. In general, the growth rate of a face is controlled by a combination of internal, structurally related factors (intermolecular bonding preferences or dislocations), and external factors (supersaturation, temperature, solvents and impurities).[28,29] The different aspect ratios of ZnO NRs result from different growth rates along the *c*-axis in different reaction media, i.e., the growth rate along the *c*-axis in ethanol is higher than those in methanol. The formation of ZnO NPs, synthesized from zinc chloride, in methanol medium is possibly

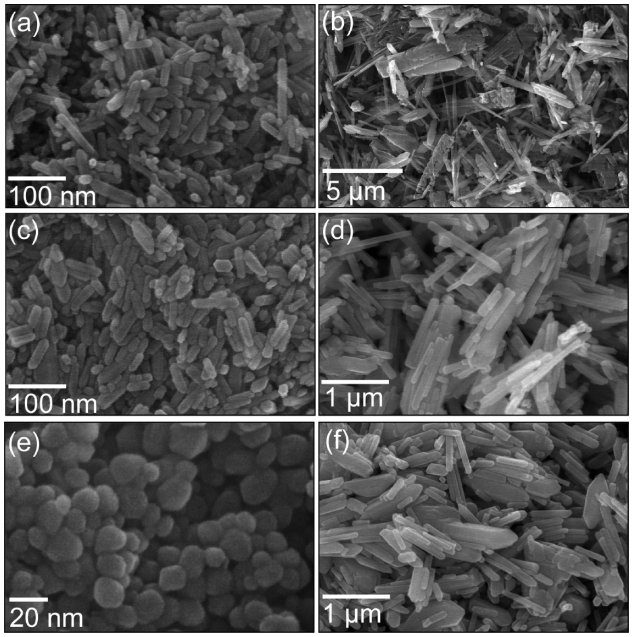

Figure 1. SEM images of ZnO nanostructures: (a) Zn-nitrate/ethanol, (b) Zn-nitrate/methanol, (c) Zn-acetate/ethanol, (d) Zn-acetate/methanol, (e) Zn-chloride/methanol, and (f) Zn-nitrate/methanol.

related to the adsorption of Cl^- ions on the Zn-terminated (0001) planes of ZnO, which eventually hindered the growth along the polar axis. Meanwhile, the same phenomenon is not occurred in ethanol, which suggests that the addition of methanol, instead of ethanol, into the growth solution may facilitate the highly electronegative Cl^- ions to adsorb preferentially on the polar ± (0001) surface.[30] However, more works need to be done for further investigation. To investigate the effect of morphology on the sensing property, we selected ZnO NRs synthesized by zinc nitrate in methanol and ZnO NPs synthesized by zinc chloride in methanol are selected for further characterization.

Morphology and structural properties of ZnO NRs and NPs are characterized by TEM. The TEM image reveals the formation of well dispersed ZnO NRs, as shown in Figure 2a.

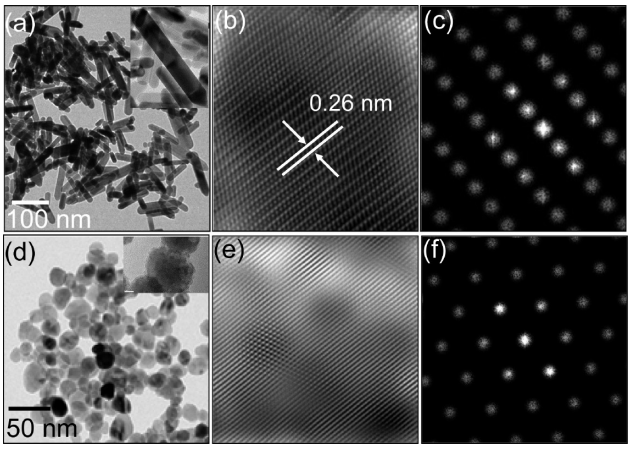

Figure 2. (a) TEM, (b) HRTEM, (c) FFT of HRTEM of ZnO NRs, and (d) TEM, (e) HRTEM, and (f) FFT of HRTEM of ZnO NPs.

The length and width of ZnO NRs vary from 100 to 150 nm and 20–25 nm, respectively. The result is in good agreement with the FESEM analysis. The HRTEM image is shown in Figure 2b, which is taken for a selected ZnO NR as displayed in Figure 2a (inset). The HRTEM image reveals that ZnO NRs are single-crystalline in nature with a spacing of 0.26 nm between two fringes, which corresponds to the (0001) plane of the bulk wurtzite ZnO crystal. The FFT pattern of corresponding HRTEM is presented in Figure 2c, which also confirms the formation of single crystalline ZnO NRs. The TEM image of ZnO NPs is shown in Figure 2d. It reveals the formation of 20–25 nm ZnO NPs, which is also comparable to FESEM result. The HRTEM images are shown in Figure 2e, which is not clear because of the agglomeration of NPs. The FFT of the selected area is presented in Figure 2f, which confirms that individual ZnO NPs are single-crystalline in nature.

XRD pattern of as prepared ZnO NRs and NPs is shown in Figure 3. All the diffraction peaks are indexed to the hexagonal wurtzite phase of ZnO (JCPDS 36–1451) and no other crystalline phases are detected. The sharp diffraction peaks suggests the good crystallinity of the both samples. Also, no other peaks related to impurity were detected in the pattern, indicating the purity of the both sample. BET surface area was calculated by using nitrogen adsorption data in the BET region ($P/P_0 < 0.3$). The surface area of ZnO NPs and NRs are 42.83 and 17.6 m^2/g, respectively.

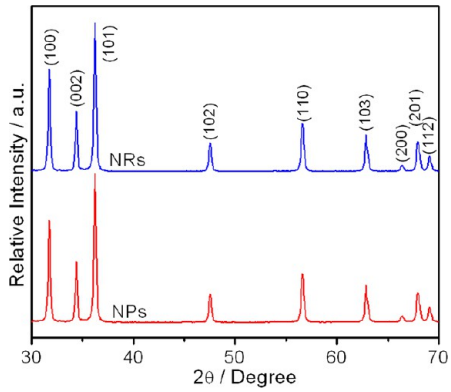

Figure 3. XRD profile of ZnO NRs and NPs.

Optical Properties. The UV–visible absorption spectra of the ZnO NRs and NPs at room temperature are displayed in Figure 4. The absorption spectra of ZnO NPs have a narrow

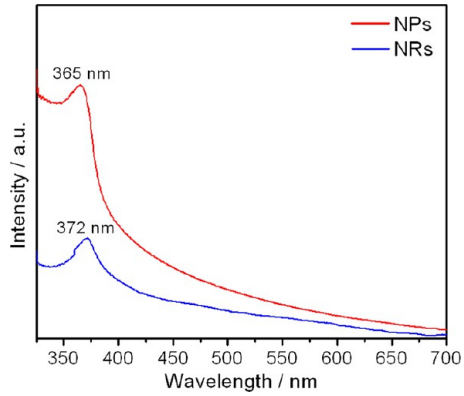

Figure 4. UV–visible spectra of ZnO NRs and NPs.

peak near the band edge in the exciton absorption region (365 nm) and blue-shifted relative to the ZnO NRs exciton absorption (372 nm). Meanwhile, both of them show a blue shift in absorption spectra as compared to bulk (380 nm). The blue shift in absorption peak is due to its nanosize, where carriers are confined in a very small district that makes the electron and hole move only in a potential well.[31]

The optical property of ZnO strongly depends on its structural property, such as crystallinity, surface state and defects. Therefore, structural property of ZnO NRs and NPs is further characterized by PL spectroscopy as shown in Figure 5. PL analysis is carried out after annealing the sample at 500 °C for 5 h, as sensing device were sintered at similar condition. The PL spectra exhibit an intense UV band around 398 nm and a weak green emission at 514 nm for ZnO NRs. The UV emission band of ZnO NPs is blue-shifted as compared to ZnO NRs and it is recorded at 388 nm. Similar to ZnO NRs, these ZnO NPs also show green emission around 514 nm (inset). The UV emission band can be explained by a near band-edge transition of wide band gap ZnO NRs, namely the free excitons recombination through an exciton–exciton collision process.[32] The blue shift in the UV emission of ZnO NPs as compared to NRs is due to the nanosize effect, as the overall particle size of ZnO NPs is smaller than ZnO NRs. The presence of weak deep-level or trap-state emissions in the green spectral region indicates that a little amount of structural defects, such as oxygen vacancies and impurities, exist in the ZnO NRs as well

dx.doi.org/10.1021/am302811h | ACS Appl. Mater. Interfaces 2013, 5, 3026–3032

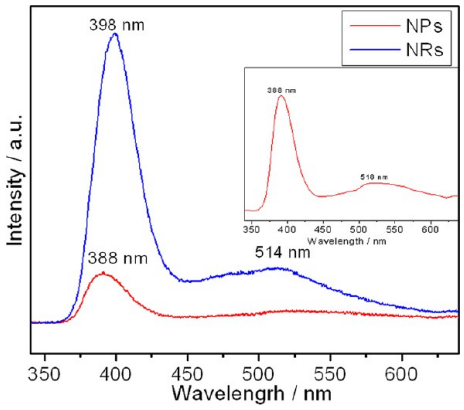

Figure 5. Room-temperature PL spectra of ZnO NRs and NPs.

as NPs.[33] It indicates that as prepared ZnO NRs and NPs have fairly good crystal quality and optical property.

Gas-Sensing Properties. Gas sensing is a surface phenomenon and it depends on various factors, such as surface area, aspect ratio, structural defects, depletion layer thickness etc. Therefore, we have investigated the effect of particle shape and size on gas-sensing property. The effect of shape and size on sensing property is investigated by comparing the NO_2-sensing property of ZnO NRs with NPs. Here, ZnO NRs and NPs, both have fairly similar diameters (20−25 nm) and they differ in their shape as well as surface area. NO_2 sensing property of these ZnO nanostructures is studied at 100 °C for 5−100 ppm of NO_2 gas. The change in resistance of ZnO NRs and NPs is shown Figure 6 for different concentrations of NO_2

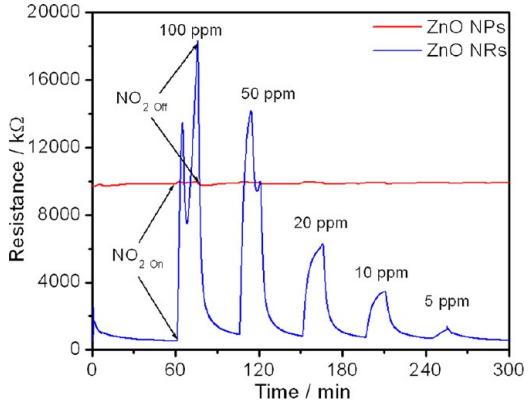

Figure 6. Resistance change of ZnO NRs and NPs at 100 °C in the presence of NO_2 gas.

gas. It can be seen that the baseline resistance of ZnO NPs is very high as compared to ZnO NRs. The response of ZnO NPs is very poor as compared to ZnO NRs. The ZnO NRs sensor showed a maximum response value is 34.8 to 100 ppm, whereas the NPs sensor showed a response of only 1.02 for NO_2 gas. However, in both cases, with increasing gas concentrations, response increases.

The gas sensing property of ZnO NRs is further tested for 5−100 ppm of NO_2 at 50−400 °C temperatures and the change in response is displayed in Figure 7. The resistance change of ZnO NRs at 300 °C for different concentrations of NO_2 gas is shown in Figure 7a. The sensor resistance increases with NO_2, reaching a nearly saturation state in a few seconds, when the probe gas is stopped, the sensor resistance decreases and recovers the initial value. It reveals both response and recovery time of ZnO NRs for NO_2 gas is fairly good. It also reveals that response increases with increasing gas concentrations. However, baseline resistance increases with decreasing testing temperatures (see Figures S2−S4 in the Supporting Information). Furthermore, response and recovery time also increases with decreasing testing temperatures (see Figure S2 and S3 in the Supporting Information). The change in response of ZnO NRs, for 5−100 ppm of NO_2, at 50−400 °C temperatures, is shown in Figure 7b. It shows that response increases with increasing gas concentrations as well as testing temperatures. However, with increasing temperatures response increases until 300 °C and then sharply decreases at 400 °C. Similarly, response increases from 5 to 50 ppm of NO_2 gas and then decreases for 100 ppm above 200 °C testing temperature. The maximum response is 44.2, recorded at 300 °C for 50 ppm of NO_2 gas. There is no big difference in response of 5 ppm of NO_2 at every testing temperature but response remarkably increases with increasing gas concentrations at high testing temperatures. From above results, it is clear that ZnO NRs are better sensing material than ZnO NPs for NO_2 gas.

Gas sensing mechanism of ZnO sensors is based on the resistance change due to the chemical and electronic interaction between the gas and the ZnO.[34] In presence of air, oxygen molecules adsorb on the surface of ZnO to form O_2^-, O^-, and O^{2-} ions by trapping electrons from the conduction band. When, the ZnO is exposed to the atmosphere of NO_2, it captures the electrons because of its higher electrophilic property leading to the formation of adsorbed NO_2^-(ads), which results in further increase in resistance. Finally, the adsorbed NO_2^- (ads) reacts with adsorbed oxygen and gives following product.

$$NO_2^-(ads) + O_2^-(ads) \rightarrow 2O^{2-}(ads) + NO_2(g) \quad (1)$$

The desorption of NO_2 molecules results in a decrease in resistance due to the release of trapped electrons on ZnO surface. After complete desorption of NO_2 molecules, the resistance reaches its initial value as shown in Figure 6.

The above-mentioned phenomenon is related to receptor function, which involves the recognition of a target gas through a gas−solid interaction that induces an electronic change of the ZnO surface. Receptor function largely depends on surface area and larger the surface area larger would be the gas interaction with solid surface. Thus, the poor response of ZnO NPs as compared to ZnO NRs, although its surface area is higher, is possibly related to transducer function. This is also supported from its very high baseline resistance, which suggests that large numbers of grain boundaries between two electrodes are present for ZnO NPs as compared to NRs. As, grain boundaries are described as highly resistive barriers, which contribute the maximum to overall device resistance. Furthermore, electrical conductivity depends on both the density and the mobility of the charge carriers in a material. The value for the mobility of the charge carriers depends on all inelastic scattering processes by which current flow is impeded. If, grain boundaries are present in a material then scattering of charge carriers at the interfaces between grains may also be possible. Therefore, the movement of an electric current in a material having grain boundaries is often far from the idealized picture under the influence of an applied electric field (Figure 8).[35] Therefore, the high baseline resistance of ZnO NPs is possibly due to the presence of higher number of grain boundaries as compared to NRs between two electrodes.

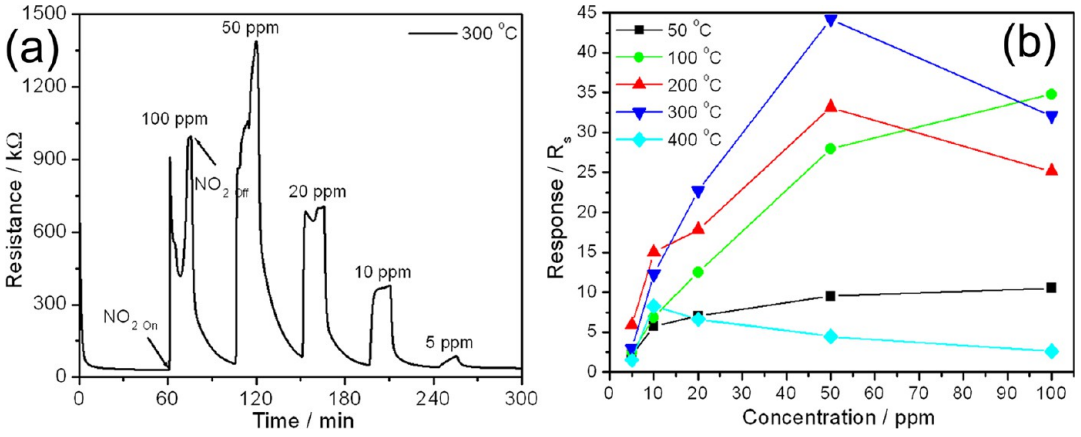

Figure 7. NO_2 gas-sensing property of ZnO NRs; (a) resistance change at 300 °C and (b) response at different temperatures (50−400 °C) and concentrations (5−100 ppm).

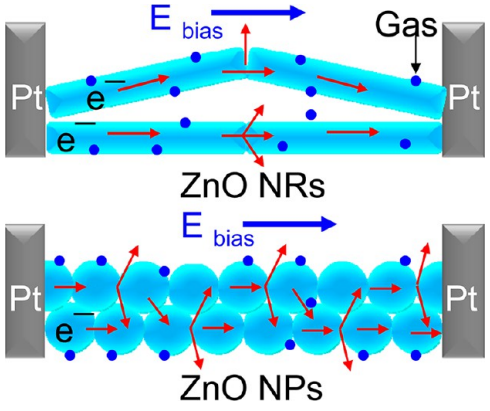

Figure 8. Conduction of current in ZnO NRs and NPs containing grain boundaries.

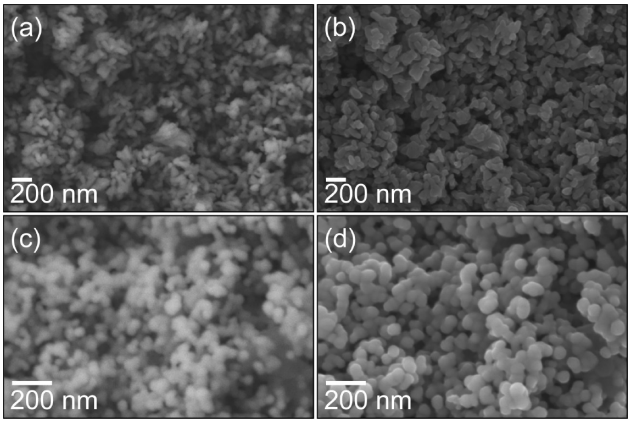

Figure 9. FESEM images ZnO thick film; (a, b) NRs and (c, d) NPs.

A relationship between numbers of grain and resistance is established by Tamaki et al., which state that resistance is directly proportional to the number of grains between two electrodes.[20−22]

$$R_a = 2R_a(\mathrm{i}) + (N-1)R_a(\mathrm{gb}) = (2R_a(\mathrm{i})) - R_a(\mathrm{gb})) + R_a(\mathrm{gb})N \quad (2)$$

Where, $R_a(\mathrm{i})$ and $R_a(\mathrm{gb})$ are resistance at interface and grain boundary in the air, respectively, and N is the number of grains included in the gap. As, the distance between two electrodes is 237 μm and diameter of both ZnO NRs and NPs are almost same (20−25 nm), therefore the numbers of grain boundaries are higher for ZnO NPs as compared to NRs (see Figure S5 in the Supporting Information). To get more information on the arrangement of particles in sensing layer, FESEM analysis is carried out and shown in Figure 9. The top view of sensing layer in Figure 9a shows that ZnO NRs are randomly placed in sensing layer, however some of them are serially connected, as well. The shape and size of ZnO NRs remained unchanged even under sintered condition at 500 °C for 5 h to fabricate sensing device. Meanwhile, more information about the contact between particles is not clear in secondary electron (SE) mode FESEM image, hence In-lens SE mode is used to get more clear topographic information as shown in Figure 9b. It reveals that ZnO NRs are well-connected to each other and no crack is found in the sensing layer. Compared to ZnO NRs, the sensing layer of NPs is also composed of uniformly distributed NPs without any change in morphology, as shown in Figure 9c. The In-lens FESEM image, in Figure 9d, exhibits that NPs are also well-connected without any crack. These images confirm that ZnO NRs form a better conduction path for charge carriers in the sensing layer than NPs, as NRs are well-connected to each other.

Thus, the lower baseline resistance (R_a) of ZnO NRs as compared to NPs is related to lesser number of grain boundaries in ZnO NRs based sensing layer. This is because some NRs are vertically aligned between the electrodes, which reduced the number of grain boundaries and therefore resistance. The NO_2 response is measured by either R_g/R_a or $(R_g - R_a)/R_a$; therefore the higher the value of R_a, the lower the response. On the contrary, CO detection by the ZnO NPs is favored because of the higher potential barrier than for the NRs.[36] The response of ZnO NRs and NPs are measured for 200−1000 ppm of CO gas at 400 °C. The response of ZnO NPs is higher than NRs as can be seen in Figure 10. The response decreases with gas concentrations in both devices. The maximum response of ZnO NPs and NRs is 7.63 and 1.8, respectively. This is because for reducing gases response is measured either by R_a/R_g or $(R_a - R_g)/R_a$. Here, R_a is higher for ZnO NPs, hence its response is also higher. Therefore, the interelectrode distance appears to affect the response irrespective of material characteristics. It also indicates that a smaller contact distance would be more preferable for gas-sensing because the resistance for sensors with a larger contact separation is high.

dx.doi.org/10.1021/am302811h | ACS Appl. Mater. Interfaces 2013, 5, 3026−3032

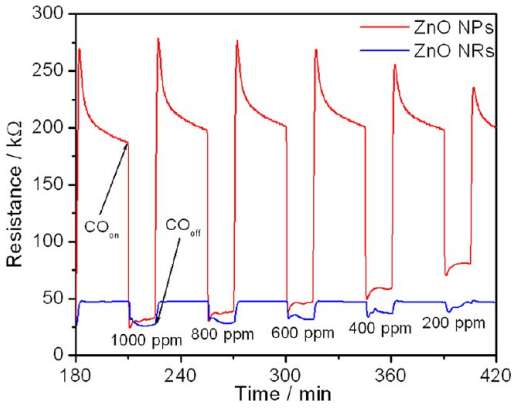

Figure 10. Resistance change of ZnO NRs and NPs at 400 °C in the presence of CO gas.

Furthermore, the increase in response for NO_2 with increasing temperatures is related to the adsorption of higher amount of oxygen and NO_2 molecules on ZnO NRs. Generally, the response increases with increasing testing temperatures for bare metal oxide. This is because the number of surface electrons increases due to thermal excitation, and therefore, a higher amount of oxygen and NO_2 molecules dissociate and adsorb on the active sites. However, the poor response of ZnO NRs for NO_2 at 400 °C is interesting, which is possibly related to the unavailability of active site for NO_2 adsorption. At higher temperature, a higher amount of oxygen molecules dissociate and adsorb on the active sites, and hence reduce the free active sites for the adsorption of NO_2 molecules, which results in poor response. It is also possible that the rate of desorption is higher than the adsorption of NO_2 at such high temperature, which results in a reduction of response. Similarly, with increasing gas concentration, the response increases, because a large amount of NO_2 molecules adsorbs, which also leads into an increase in resistance change that results in an increase in response. However, the poor response of ZnO NRs for 100 ppm of NO_2, above 200 °C, can be explained by the competition between the adsorption sites and the concentration of target gas. In low gas concentrations, the surface reactions are linearly dependent on the NO_2 concentrations as long as adsorption sites are enough. When, the NO_2 concentrations exceed the available adsorption sites on the surface of ZnO then NO_2 molecules have to compete for adsorption sites and it becomes the rate-determining step for high gas concentrations. With increasing temperatures, active sites are already adsorbed by oxygen ions, which further reduced the adsorption sites for NO_2; therefore, the response decreases at high temperatures for high concentrations of gas.

As shown in Figure 7a, the difference in baseline resistance of ZnO NRs at different temperatures is interesting and need to be explained (see Figure S2−S4 in the Supporting Information). The baseline resistance in metal oxide depends on electron transport and formation of depletion layer due to dissociation and adsorption of oxygen molecules. If the influence of oxygen adsorption and desorption is ignored, then it is mainly determined by the manner in which electron transport takes place. The electron transport in metal oxide sensor can take place either by tunneling transport or migration transport. Tunneling transport occurs only when grains are in point contact, which involves no neck formation. However, tunneling transport in between grains is possible only when the gaps are very small (0.01 nm), and therefore, tunneling transport is temperature independent, whereas if grains form a small neck, then migration transport takes place, and therefore, migration transport is temperature-dependent. Thus, in metal oxide gas sensors, mostly migration transport is involved.[37] If we consider a migration transport path with resistance (R_m), then R_m increases exponentially according to eq 3

$$R_m = R_{mo}\exp^{(eV_s/RT)} \quad (3)$$

Where V_s is double Schottky barrier height, RT is thermal energy, and R_{mo} is resistance at V_s = 0. Therefore, baseline resistance increases with decreasing temperatures.

The poor recovery time at low temperatures as compared to high temperatures for NO_2 can be explained by slow desorption of gas at low temperatures. Also, this drift is possibly related to slow reactions within chemical species at low temperatures as compared to high temperatures.

More interestingly, we found spike at every test for NO_2 gas, especially at high temperatures for high concentrations of NO_2 gas as shown in Figures 6 and 7a. Although the exact reason for the origin of spike is not well understood, it is believed that it is related to the dissociation of adsorbed NO_2 to adsorb NO and O on the ZnO surface. Spencer et al. described that NO_2 can readily dissociate into O and NO over the defect surface with an O-vacancy.[38]

$$NO_2(\text{abs}) \rightarrow NO(\text{ads}) + O(\text{ads}) \quad (4)$$

It is evident from PL spectroscopy that these ZnO nanostructures have little structural defects, which is possibly related to oxygen vacancies. Therefore, it is possible that spikes in sensor signal appear due to multiple adsorptions. First, NO_2 molecules adsorb on ZnO surface by capturing the electrons and hence resistance increases. When dissociation of these adsorbed NO_2 molecules start then resistance decreases. Simultaneously, dissociated NO_2 species (NO and O) start adsorption on ZnO surface by capturing the electrons and thus resistance further increases.

CONCLUSIONS

Single-crystalline ZnO NRs with 20−25 nm diameter and 100−150 nm length were successfully synthesized by solvothermal method. It was found that the shape and size greatly affected the response and the response of ZnO NRs was higher than ZnO NPs for NO_2 and vice versa for CO gases. The response of these ZnO NRs for NO_2 was very high (44.2 to 50 ppm at 300 °C) and increased with working temperatures as well as concentrations. The response of ZnO NRs was about 30 times higher than ZnO NPs at 100 °C. On the other hand, the response of ZnO NPs for CO gas was 4 times higher than NRs at 400 °C. It was demonstrated that the higher response of ZnO NRs as compared to NPs for NO_2 gas was related to the transducer factor, as a large number of grain boundaries in the case of NPs increased the resistance and lowered the response.

ASSOCIATED CONTENT

Supporting Information

Sensor device fabrication, resistance change of ZnO NRs for NO_2 gas at various temperatures, and scheme of arrangement of NPs and NRs in sensing layer is provided. This material is available free of charge via the Internet at http://pubs.acs.org/.

AUTHOR INFORMATION

Corresponding Author

*E-mail: yeontae@jbnu.ac.kr. Tel: +82-63-270-2288. Fax: +82-63-270-2305.

Notes

The authors declare no competing financial interest.

ACKNOWLEDGMENTS

This paper was supported by research funds of Chonbuk National University in 2012 and National Research Foundation (NRF) grant funded by the Korea government (MEST) (NRF-2010-0019626, 2012R1A2A010067873).

REFERENCES

(1) Rajendra Kumar, R. T.; Grabowska, J.; Mosnier, J. P.; Henry, M. O.; McGlynn, E. *Superlattice Microstruct.* **2007**, *42*, 337−342.
(2) Sberveglieri, G.; Barrato, C.; Comini, E.; Faglia, G.; Ferroni, M.; Ponzani, A.; Vomiero, A. *Sens. Actuators, B* **2007**, *121*, 208−213.
(3) Rella, R.; Siciliano, P.; Capone, S.; Epifani, M.; Vasanelli, L.; Licciulli, A. *Sens. Actuators, B* **1999**, *58*, 283−288.
(4) Yamazoe, N.; Shimanoe, K. *J. Electrochem. Soc.* **2008**, *155*, J85−J92.
(5) Chaabouni, F.; Abaab, M.; Rezig, B. *Sens. Actuators, B* **2004**, *100*, 200−204.
(6) Comini, E.; Baratto, C.; Faglia, C.; Ferroni, M.; Sbverglieri, G. *J. Phys. D Appl. Phys.* **2007**, *40*, 7255−7259.
(7) Carney, C. M.; Yoo, S.; Akbar, S. A. *Sens. Actuators, B* **2005**, *108*, 29−33.
(8) Comini, E.; Faglia, G.; Sberveglier, G.; Pan, Z.; Wang, Z. L. *Appl. Phys. Lett.* **2002**, *81*, 1869.
(9) Tsukazaki, A.; Ohtomo, A.; Onuma, T.; Ohtani, M.; Makino, T.; Sumiya, M.; Ohtani, K.; Chichibu, S. F.; Fuke, S.; Segawa, Y.; Ohno, H.; Koinuma, H.; Kawasaki, M. *Nat. Mater.* **2005**, *4*, 42−46.
(10) Wang, Z. L. *J. Phys.: Condens. Matter* **2004**, *16*, R829−R858.
(11) Janotti, A.; Van de Walle, C. G. *Rep. Prog. Phys.* **2009**, *72*, 126501.
(12) Chu, D.; Masuda, Y.; Ohji, T.; Kato, K. *Langmuir* **2010**, *26*, 2811−2815.
(13) Xu, J.; Pan, Q.; Shun, Y.; Tian, Z. *Sens. Actuators B Chem.* **2000**, *66*, 277−279.
(14) Brayner, R.; Ferrari-Iliou, R.; Brivois, N.; Djediat, S.; Benedetti, M. F.; Fievet, F. *Nano Lett.* **2006**, *6*, 866−870.
(15) Yi, G.-C.; Wang, C.; Park, W. *Semicond. Sci. Technol.* **2005**, *20*, S22−S34.
(16) Lu, C.; Qi, L.; Yang, J.; Tang, L.; Zhang, D.; Ma, J. *Chem. Commun.* **2006**, *33*, 3551−3553.
(17) Wang, D.; Song, C. *J. Phys. Chem. B* **2005**, *109*, 12697−12700.
(18) Cheng, B.; Samulski, E. T. *Chem.Commun.* **2004**, 986−987.
(19) Yamazoe, N.; Sakai, G.; Shimanoe, K. *Catal. Surv. Asia* **2003**, *7*, 63−75.
(20) Tamaki, J.; Nakataya, Y.; Konishi, S. *Sens. Actuators B Chem.* **2008**, *130*, 400−404.
(21) Tamaki, J.; Niimi, J.; Ogura, S.; Konishi, S. *Sens. Actuators B Chem.* **2006**, *117*, 353−358.
(22) Tamaki, J.; Miyaji, A.; Makinodan, J.; Ogura, S.; Konishi, S. *Sens. Actuators B Chem.* **2005**, *108*, 202−206.
(23) Williams, D. E. *Sens. Actuators, B* **1999**, *57*, 1−16.
(24) Scott, R. W. J.; Yang, S. M.; Chabanis, G.; Coombs, N.; Williams, D. E.; Ozin, G. A. *Adv. Mater.* **2001**, *13*, 1468−1472.
(25) McAleer, J. F.; Moseley, P. T.; Norris, J. O. W.; Williams, D. E. *J. Chem. Soc., Faraday Trans.* **1987**, *1*, 1323−1346.
(26) Rai, P.; Yu, Y.-T. *Sens. Actuators, B* **2012**, *161*, 748−754.
(27) Li, W.; Shi, E.; Zhong, W.; Yin, Z. *J. Cryst. Growth* **1999**, *203*, 186−196.
(28) Ter Horst, J. H.; Geertman, R. M.; van Rosmalen, G. M. *J. Cryst. Growth* **2001**, *230*, 277−284.
(29) Wong, E. M.; Bonevich, J. E.; Searson, P. C. *J. Phys. Chem. B* **1998**, *102*, 7770−7775.
(30) Wu, K.; Sun, Z.; Cui, J. *Cryst. Growth Des.* **2012**, *12*, 2864−2871.
(31) Buhro, W. E.; Colvin, V. L. *Nat. Mater.* **2003**, *2*, 138−139.
(32) Kong, Y. C.; Yu, D. P.; Zhang, B.; Fang, W.; Feng, S. Q. *Appl. Phys. Lett.* **2001**, *78*, 407.
(33) Djurišić, A. B.; Leung, Y. H. *Small* **2006**, *2*, 944−961.
(34) Bai, S.; Chen, L.; Li, D.; Yang, W.; Yang, P.; Liu, Z.; Chen, A.; Chung, C. L. *Sens. Actuators B Chem.* **2010**, *146*, 129−137.
(35) Hernandez-Ramirez, F.; Prades, J. D.; Jimenez-Diaz, R.; Fischer, T.; Romano-Rodriguez, A.; Mathur, S.; Morante, J. R. *Phys. Chem. Chem. Phys.* **2009**, *11*, 7105−7110.
(36) Carotta, M. C.; Cervi, A.; di Natale, V.; Gherardi, S.; Giberti, A.; Guidi, V.; Puzzovio, D.; Vendemiati, B.; Martinelli, G.; Sacerdoti, M.; Calestani, D.; Zappettini, A.; Zha, M.; Zanotti, L. *Sens. Actuators, B* **2009**, *137*, 164−169.
(37) Yamazoe, N.; Shimanoe, K.; Sawada, C. *Thin Solid Films* **2007**, *515*, 8302−8309.
(38) Spencer, M. J. S.; Yarovsky, I. *J. Phys. Chem. C* **2010**, *114*, 10881−10893.